Metadynamical approach to the generation of amorphous structures: The case of *a*-Si:H

Parthapratim Biswas,[1,*] Raymond Atta-Fynn,[2,†] and Stephen R. Elliott[3,‡]

[1]*Department of Physics and Astronomy, University of Southern Mississippi, Hattiesburg, Mississippi 39406, USA*

[2]*Department of Physics and Astronomy, University of Texas, Arlington, Texas 76006, USA*

[3]*Department of Chemistry, University of Cambridge, Cambridge CB2 1EW, United Kingdom*

(Received 15 March 2016; published 25 May 2016)

We present a dynamical approach to generate defect-free continuous-random-network (CRN) models of hydrogenated amorphous silicon (*a*-Si:H). Using the atomic coordination number of silicon as a collective variable and few configurational constraints, we have shown that classical metadynamics can be used to construct CRN models of *a*-Si with arbitrary concentrations of dangling-bond coordination defects. These defective networks have been subsequently hydrogenated to produce high-quality models of *a*-Si:H using *ab initio* total-energy calculations to generate hydrogen (H) microstructures for H concentrations from 7 to 22 at. %. The structural, electronic, optical, and vibrational properties of the models are examined, and the microstructure of the hydrogen distribution is analyzed and compared with experimental data from neutron scattering, spectroscopic ellipsometry, infrared spectroscopy, and nuclear magnetic resonance studies. The results obtained from the models are found to be in excellent agreement with the experimental data.

DOI: 10.1103/PhysRevB.93.184202

I. INTRODUCTION

Atomistic models of many amorphous semiconductors are well represented by continuous random networks (CRNs) [1]. Despite the simplicity of the CRN model, the dynamic modeling of high-quality CRNs (i.e., with low strain and few structural defects) has proved to be particularly difficult. While a few event-based approaches, such as the Wooten-Winer-Weaire (WWW) [2] and activation-relaxation (ART) techniques [3], can address the problem satisfactorily, we are not aware of any molecular-dynamical approaches that can produce high-quality continuous random networks for modeling tetrahedral semiconductors. Conventional *ab initio* molecular dynamics (AIMD) [4–7] and Car-Parinello (CP) approaches [8] have been employed successfully to study structural glasses via traditional "melt-quench" approaches, but their use is limited mostly to amorphous solids with strong *glassy* behavior. For amorphous materials with no or weak glassy behavior (e.g., *a*-Si, *a*-Ge, and *a*-Si:H), MD simulations either produce highly defective configurations or tend to crystallize the system during quenching from molten states at high temperature. The large computational cost of AIMD, combined with the resulting high defect concentrations, has been a major obstacle for accurate first-principles studies of amorphous solids with no or weak glassy behavior, especially on the intermediate-range length scale.

In this paper, we present a dynamical approach for structural modeling of hydrogenated amorphous silicon (*a*-Si:H), an important electroactive and photovoltaic material of technological importance [9–12]. Recent developments of high-efficiency solar cells, based on *a*-Si:H/*c*-Si heterojunctions with intrinsic thin-layer (HIT) technology, are indicative of the continuous importance of the material in photovoltaics [13–16]. Here, we have shown that a dynamical approach can be developed to generate amorphous networks by including a bias potential in the total energy using a variant of accelerated molecular-dynamics simulations, known as metadynamics [17,18]. The resulting networks can be passivated with hydrogen to produce hydride configurations of amorphous silicon. A notable feature of the approach is its ability to control the coordination number of the atoms in order to produce different silicon-hydrogen bonding configurations, which are consistent with experimental data from infrared (IR) spectroscopy [19–22] and nuclear magnetic resonances (NMR) [23–26]. This renders the generation of high-quality *a*-Si:H models possible with no defects for a range of hydrogen concentration and system sizes of up to several thousand atoms. While the emphasis of the present work is on *a*-Si:H, the approach can be readily generalized to produce a variety of binary and ternary amorphous networks in two and three dimensions, and amorphous/crystalline heterojunctions. Below, we briefly mention the existing modeling methods and their disadvantages before addressing the new approach and its application to *a*-Si:H.

The conventional routes to structural modeling of *a*-Si:H are mostly dominated by static approaches coupled with *ab initio* relaxations [4–8,27–29]. Here, one usually proceeds by building models of *a*-Si, via WWW [2], ART [3], or otherwise [30–32], which are subsequently hydrogenated and relaxed to obtain configurations at stable local minima using *ab initio* total-energy optimizations. However, in the absence of thermal motion, hydrogen atoms can relax only locally and are unlikely to move between different trap centers, leading to a poor distribution of hydrogen in the network [33]. The standard remedy is to subject the system to a medium-temperature (600–800 K) *ab initio* molecular dynamics run, so that hydrogen in the network can be redistributed to attain an "equilibrium" distribution. *Ab initio* molecular dynamics, however, is computationally expensive, and it is unclear whether the short-time dynamics (of several picoseconds for large systems) would suffice to capture the standard picture of hydrogen migration, namely hopping of hydrogen atoms from traps to high-energy transport sites

*partha.biswas@usm.edu

†attafynn@uta.edu

‡sre1@cam.ac.uk

and back into traps again [34,35]. A consensus is that *ab initio* simulations with a simulation time of a few tens of picoseconds might be sufficient for small systems to produce the correct *global* physical observables (such as 2- and 3-body correlations, the average coordination number, and electronic density of states [7]), but for large systems, the approach is computationally infeasible and unlikely to produce correct local properties, such as vacancies [36,37], voids [31,32,38], and molecular hydrogen [31,39]. In summary, the major disadvantages of current dynamical approaches include the high computational cost and the production of a large density of coordination defects. Since device-quality samples of a-Si:H have a typical defect concentration of order 10^{16} cm^{-3} (i.e., 1 in 10^7 atoms), ideal models of a-Si:H must be practically free from any defects in order to represent laboratory-grown samples realistically. To this end, we present here a dynamical approach, which is capable of producing large realistic models of a-Si:H with practically no coordination defects for a wide range of hydrogen concentrations.

The plan of the paper is as follows. In Sec. II, we address the generation of amorphous-silicon networks using metadynamics, which is followed by hydrogen passivation, equilibration, quenching, and relaxation of the hydrogenated networks. Section III discusses results for structural, electronic, optical, and vibrational properties by comparing our results with neutron diffraction [40], nuclear magnetic resonance [23–26], spectroscopic ellipsometry [41], and infrared spectroscopy [21,42] studies. This is followed by conclusions of the work in Sec. IV.

II. COMPUTATIONAL METHOD

The dynamical approach developed here consists of the following steps: (1) adaptation of classical metadynamics using appropriate collective variables to generate a-Si networks with coordination defects to incorporate hydride configurations consistent with experimental data; (2) hydrogenation of dangling bonds (1-, 2-, and 3-fold coordinated Si atoms); (3) *ab initio* molecular dynamics comprising equilibration of the resulting hydride configurations at 800 K for 20 ps, followed by quenching the systems from 800 K to 300 K in 25 ps (5 ps per 100 K); (4) *ab initio* total-energy relaxations via the conjugate-gradient method to obtain the final structure at a stable local minimum.

A. Metadynamics

The first step involves metadynamical simulations of amorphous-silicon networks with a requisite defect density. This can be readily implemented once a set of collective variables is identified for the problem. Metadynamics [17,18] is a nonequilibrium MD approach for an accelerated sampling of the events on the free-energy surface (FES) associated with a set of collective variables. The collective variables, $\Xi(\mathbf{R}^N)$, are continuous and differentiable functions of the system coordinates $\mathbf{R}^N$, the choice of which is guided by the physical events to be studied in a problem. Once the collective variables are determined, the accelerated sampling is achieved by adding a history- and time-dependent bias potential, $V(\Xi,t)$, to the total energy of the system. The bias is applied adaptively during the time evolution of the system by adding a repulsive Gaussian potential centered on the current position of Ξ at a regular time interval of τ_G. The accumulation of the Gaussian-bias potentials progressively flattens the FES, and facilitates the system in overcoming the energy barriers or escaping from the potential minima at an accelerated rate. The presence of a history-dependent bias constrains the system to explore new regions of the FES. Thus, by choosing a set of appropriate collective variables, it is possible to study the desired configurations of interest for the problem. For an arbitrary value ξ, of Ξ at time t, the Gaussian-bias potential $V(\xi,t)$ is given by

$$V(\xi,t) = \sum_{\substack{t' = \tau_g, 2\tau_g, \ldots \\ t' < t}} H_g \exp\left(-\frac{|\xi - \Xi(t')|^2}{2\omega^2}\right), \qquad (1)$$

where H_g and ω are the Gaussian height and width of the bias potential, respectively. The basic assumption in metadynamics is that the free-energy function is Gaussian-representable; i.e., after a sufficiently long time, $V(\xi,t)$ cancels the underlying free energy $F(\xi)$ along Ξ, and is given by the negative of the accumulated bias up to a constant value,

$$F(\xi) \approx -\lim_{t\to+\infty} V(\xi,t) + \text{constant}. \qquad (2)$$

Here, we have used the average coordination number of silicon atoms as a collective variable to generate an ensemble of continuous random networks with varying (coordination) defect concentrations. This enables us to produce a-Si networks with a requisite number of dangling bonds to construct SiH/SiH$_2$ configurations via hydrogenation, which are consistent with experimental data from infrared spectroscopy [20,22,38,42]. For a system with N silicon atoms, the collective variable ξ can be written as

$$\xi = \frac{1}{N}\sum_{i=1}^{N}\sum_{\substack{j=1 \\ j\neq i}}^{N} \Theta(r_{ij}) \qquad (3)$$

where

$$\Theta(r_{ij}) = \begin{cases} 1, & \text{if } r_{ij} \leqslant r_1, \\ \frac{1}{2}\left[1 + \cos\left(\frac{\pi(r_{ij}-r_1)}{r_2-r_1}\right)\right], & \text{if } r_1 < r_{ij} \leqslant r_2, \\ 0, & \text{if } r_{ij} > r_2, \end{cases} \qquad (4)$$

is a continuous nearest-neighbor function that decays monotonically beyond the first shell of neighbors, and r_1 and r_2 are the upper and lower limits of the first and second nearest-neighbor distances, respectively [43].

All metadynamical runs were performed with a system size of $N = 1000$ silicon atoms using the modified Stillinger-Weber potential [44,45]. Starting from a random initial configuration, the system was equilibrated at a constant initial temperature of 1600 K for 250 ps with a time step of 1 fs using a chain of Nosé-Hoover thermostats [46–48]. Next, the temperature of the system was reduced from 1600 K to 1000 K in two steps (300 K per step). At each step, the temperature was kept constant for a period of 250 ps. At the end of the 1000 K run, the Gaussian potential was switched on to initiate metadynamics using the following (metadynamics) parameters: Gaussian-addition rate $1/\tau_G = 1$ ps^{-1} (i.e., addition of a Gaussian kernel or function at

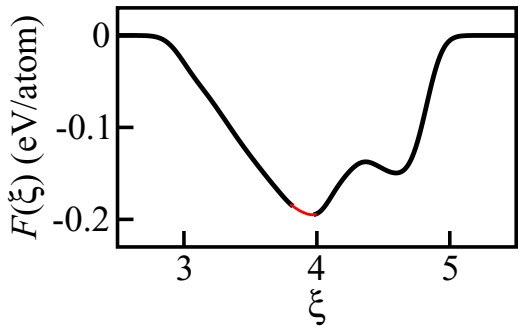

FIG. 1. The free energy of a-Si from metadynamical simulations at 1000 K as a function of the collective variable ξ. The thin red curve indicates the region (of ξ) from where the configurations of a-Si have been sampled for hydrogenation.

a time interval of 1 ps), Gaussian height $H_G = 0.1$ eV, Gaussian width $\omega = 0.1$, and the cutoff distances (for the nearest-neighbor function) $r_1 = 2.7$ Å and $r_2 = 3.15$ Å (see Eq. (4) and Ref. [43]).

During metadynamical runs, several hundred configurations of the system along the trajectory with 4-, 3-, and 2-fold coordinated Si atoms were collected to generate a-Si:H models for a range of concentrations. Metadynamics can produce configurations with under- and over-coordinated defects, so care was taken to ensure that the configurations collected for hydrogenation contained only under-coordinated defects. Specifically, the configurations consisted of at least 77% 4-fold coordinated atoms, 21% 3-fold, and 2% 2-fold coordinated atoms, which were sufficient to generate models in a wide concentration range of 7–22 at. % of hydrogen. Figure 1 shows a plot of the free-energy function $F(\xi)$ of a-Si as a function of the collective variable ξ from metadynamical simulations. The thin red curve denotes the region, $3.75 \leqslant \xi \leqslant 4$, of the free energy from where the aforementioned configurations were collected for subsequent hydrogenation. This region of ξ corresponds to mostly 3-fold coordinated dangling bonds with an admixture of a few 2-fold and 1-fold coordinated Si atoms [49]. While several hundreds of such configurations were collected for statistical purposes, we confined ourselves to seven representative configurations for each hydrogen concentration of interest for the purpose of configurational averaging of the physical quantities presented here.

It should be noted that the free-energy values, associated with the collective variable ξ, shown in Fig. 1 are not necessarily converged. Since the purpose of metadynamics simulations here is to generate configurations with specific topological properties (e.g., dangling-bond defects), our metadynamic simulations ended as soon as an appropriate number of specific configurations were collected. Thus, the free-energy values presented in Fig. 1 do not necessarily reflect the limiting value of $V(\xi,t)$ in the long-time limit as required by Eq. (2). Furthermore, the total number of Gaussian functions that is necessary to produce the required configurations may vary significantly. This depends on the height and width of the Gaussian potential, the complexity of the potential energy landscape, and the stability of initial configurations to be used for metadynamics simulations.

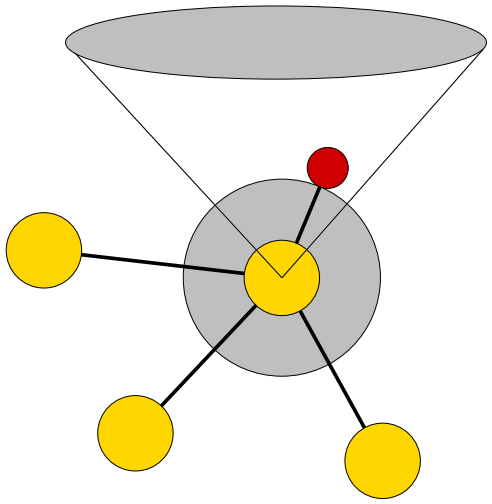

FIG. 2. Hydrogenation of a 3-fold dangling bond. A hydrogen atom (red) is placed on the surface of a central sphere (gray), whose center coincides with that of a defective Si atom (yellow), such that the Si-H bond retains the maximal tetrahedral character of the site.

B. Hydrogenation

Hydrogenation proceeds by passivating dangling bonds. As mentioned earlier, none of the configurations collected during metadynamical simulations has over-coordinated bonds, but mostly 2- and 3-fold coordinated dangling bonds. Thus, to passivate a configuration efficiently, the defect sites were identified and a hypothetical sphere of radius 1.0–1.2 Å was constructed around each site [50]. Next, hydrogen atoms were placed on the surface of the sphere such that the tetrahedral character of the defect site was maintained maximally. To this end, an ensemble of unit radial vectors was generated in a fine mesh within a cone of solid angle Ω, and a direction vector was identified for placing a hydrogen atom along the vector (see Fig. 2). The latter was chosen to ensure that the average bond angle and its root-mean-square (rms) deviation at the defect site remained as close as possible to 109.5° and less than 12°, respectively, to maintain the tetrahedral quality of the network. The rms deviation was varied from 5° to 12° by 0.5° increments in each sweep (of radial vectors) until a suitable direction was identified. This was done by calculating the average bond angle and its rms deviation for the defect site for each direction until they satisfy the criteria mentioned above. The procedure is illustrated in Fig. 2 by passivating a dangling bond with a hydrogen atom. For a dangling bond with two missing Si atoms, two H atoms were added successively to ensure that the tetrahedral character of the defect site was maintained. The procedure was repeated for all defect sites to complete the hydrogenation process.

C. *Ab initio* dynamics and relaxation

Upon successful hydrogenation, the configurations were subjected to the following steps: (a) relaxation of the total energy to reduce the strain associated with the addition of hydrogen atoms; (b) equilibration of the resulting configurations at 800 K for 20 ps to facilitate hydrogen migration; (c) cooling the equilibrated configurations from 800 K to 300 K in 25 ps

to obtain an equilibrium distribution of hydrogen; (d) a further total-energy relaxation via the conjugate-gradient method to obtain a stable local minimum. Step (c) was performed by reducing the temperature of the systems from 800 K to 300 K in steps of 100 K in 5 ps. The annealing and quenching of the hydrogenated networks were performed within the framework of density-functional theory using the code SIESTA [51]. A time step of 1 fs was used to integrate the equations of motion. The temperature of the system was controlled by the Nosé thermostat [46]. SIESTA uses pseudopotentials and localized basis functions for solving the Kohn-Sham equations. We employed double-ζ basis functions to expand the Kohn-Sham orbitals for silicon and hydrogen. Electronic correlations were taken into account via the local-density approximation (LDA) [52] using the Perdew-Zunger formulation [52]. SIESTA employs norm-conserving Troullier-Martins pseudopotentials [53], which are factorized into the Kleinmann-Bylander form [54]. Due to large system sizes ($>$ 1000 atoms) and long MD simulation times (45 ps per configuration), the Kohn-Sham equations were solved in a non-self-consistent manner using the Harris functional [55]. To obtain the final structure and equilibrium mass density for each concentration, the atomic positions and cell-lattice vectors were simultaneously relaxed using the conjugate-gradient method until the force on each atom was less than 0.005 eV/Å and the stress was less than 0.1 GPa.

III. RESULTS AND DISCUSSION

This section addresses structural, electronic, optical, and vibrational properties of the models for different hydrogen concentrations. Microstructural properties of hydrogen distributions are examined, and addressed by comparing the results from the models with those from nuclear magnetic resonance [23–26] and infrared absorption [20–22,42] studies.

A. Structural properties

We begin by addressing the variation of the mass density of a-Si:H with hydrogen concentration. Theoretical studies often ignore this variation by assuming the experimental density of a-Si:H as a simulation parameter. However, the density of a-Si:H depends on the hydrogen concentration and should be treated as a variable in simulations. Figure 3 shows the density

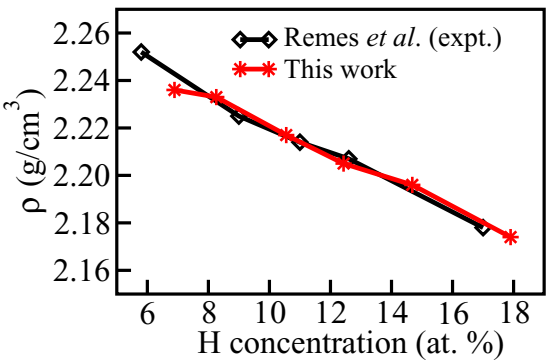

FIG. 3. Mass density of model networks of a-Si:H versus hydrogen concentration. Experimental data from Ref. [56] are included for comparison.

TABLE I. Summary of structural properties of a-Si:H models: system sizes (N), atomic H concentration (H_{conc}), density (ρ), average Si-Si bond length ($r_{Si\text{-}Si}$), average Si-H bond length ($r_{Si\text{-}H}$), average bond angle ($\langle\theta\rangle$), rms deviation of bond angles ($\Delta\theta_{rms}$), and the percentage of 4-fold Si atoms (CN_{Si}).

N	ρ (g cm^{-3})	H_{conc} (at. %)	$r_{Si\text{-}Si}$ (Å)	$r_{Si\text{-}H}$ (Å)	$\Delta\theta_{rms}$	$\langle\theta\rangle$ (degrees)	CN_{Si} (%)
1074	2.236	6.9	2.38	1.51	9.44	109.20	99.9
1090	2.233	8.3	2.38	1.52	9.63	109.19	99.9
1118	2.217	10.6	2.38	1.51	9.22	109.17	99.8
1142	2.205	12.4	2.38	1.51	9.23	109.16	100
1172	2.196	14.7	2.38	1.51	9.31	109.12	99.9
1218	2.174	17.9	2.37	1.51	9.54	109.11	100
1282	2.165	22.0	2.37	1.51	10.04	109.02	99.8

of a-Si:H models for different hydrogen concentrations, along with the experimental density of variously prepared a-Si:H films reported in Ref. [56]. Although the exact density of a-Si:H films depends upon the method of preparation, history of the samples, and the deposition conditions, infrared measurements suggest that the density of a-Si:H decreases with an increase of the hydrogen content [56]. A comparison of our results with the experimental data from Fourier-transform IR measurements [56] confirms that the variation is correctly reflected in our results. We should mention at this point that the use of double-ζ basis functions for Si and H atoms is very important for producing the correct density of a-Si:H, as observed in experiments for varying hydrogen concentrations. Our present and earlier works [57] suggest that a single-ζ basis (for Si) can produce reasonably good structural and electronic properties provided one uses the experimental density (for a given concentration) as an input simulation parameter in the construction of the simulation cell for a given number of atoms.

Table I lists the key structural properties of the models for concentrations from 7 to 22 at. % of hydrogen. The models are practically free from coordination defects (see CN_{Si} in column 8, Table I), and the average values of the bond angles are close to the ideal tetrahedral value of 109.47°, with an rms deviation of 9.4°–10.1°. The latter matches closely with the computational [58] and experimental [59] values of 9.8° and 9.6°, respectively.

In Fig. 4, the correlation function [60] $T(r) = J(r)/r$, where $J(r)$ is the total radial distribution function, is shown, together with the results from neutron scattering experiments by Wright *et al.* [40]. The agreement between computed values and experimental data is quite remarkable, which ensures the reliability of the models as far as the 2-body correlations are concerned. This observation can be combined with the results from Table I to conclude that the structural properties of a-Si:H have been produced accurately in our approach.

The effect of hydrogen on the connectivity of a-Si:H networks has been analyzed by studying the distribution of irreducible rings [34] and the number of tetrahedral units and their volume distribution associated with silicon atoms. The addition of hydrogen in a-Si networks leads to the formation of large ring structures, especially at high H concentrations. As

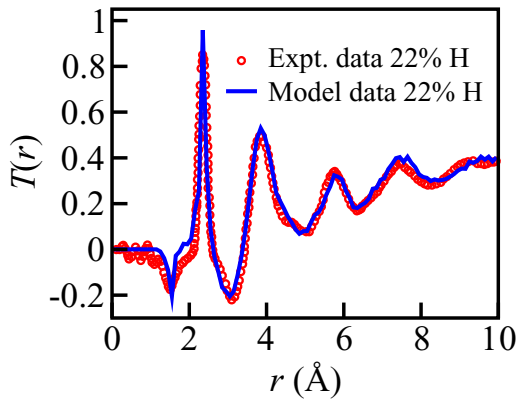

FIG. 4. Neutron-weighted correlation functions (atoms/Å^2) of a-Si:H from a 1000-Si-atom model (blue) with 22 at. % hydrogen and experiments. Experimental data (red) correspond to 22 at. % of hydrogen from Ref. [40].

more hydrogen atoms begin to bond with silicon atoms at high H concentrations, irreducible closed paths (or rings) associated with singly-coordinated H atoms become longer. Thus, the ring distribution can be expected to be correlated with the concentration of hydrogen and the density of SiH_n ($n = 1$, 2, 3) configurations. This is reflected in Fig. 5—although in a subtle way—where the irreducible-ring distributions for two models are plotted as a function of their ring sizes. A comparison of the ring-size distributions at low (6.9 at. %) and high (22 at. %) H concentrations shows that the number of large rings has increased slightly as the concentration of hydrogen increases and supports this assumption. The minor changes in the ring distributions can be explained as being due to the absence of significant numbers of di- and trihydride configurations. In a recent publication [31], we have shown that the change is particularly noticeable in large models at high H concentrations where the hydrogen microstructure is

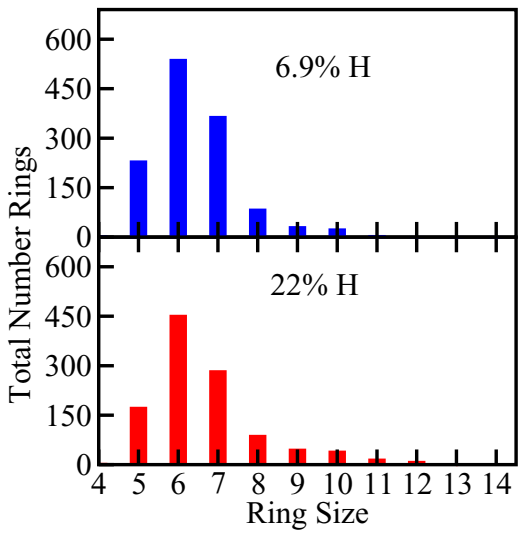

FIG. 5. Irreducible-ring distribution versus ring sizes for two models with different H concentrations. Hydrogenation causes a subtle change in the number of rings at a high concentration of hydrogen.

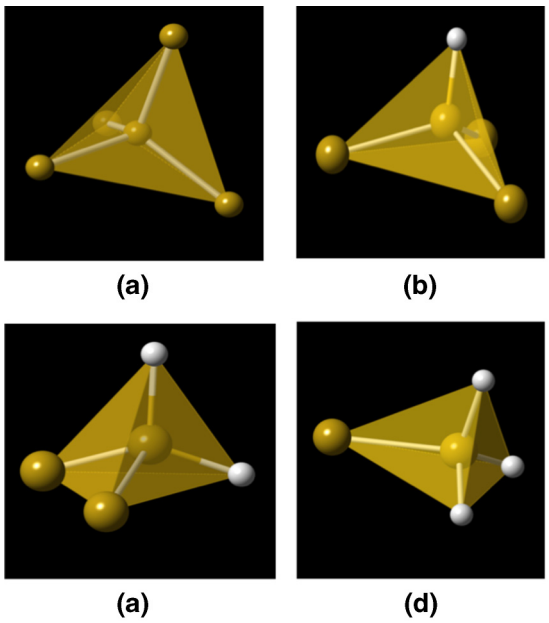

FIG. 6. Tetrahedral units associated with $Si_{4-n}H_n$ configurations for $n = 0$, 1, 2, 3. Silicon and hydrogen atoms are shown in yellow and white colors, respectively.

characterized by the copious presence of di- and trihydride configurations, as well as microvoids in the network.

While irreducible rings reflect the medium-range topological changes in the structure due to hydrogen incorporation, structural changes associated with the nearest neighbors of silicon atoms can be quantified by the distribution of tetrahedral volumes of local silicon tetrahedra (formed by the four nearest neighbors of each Si atom). Since the volume of an irregular tetrahedron depends on the length of its six edges (via the four nearest-neighbor distances) and the six angles subtended by the four vertices at the center of the tetrahedron, the volume distribution of silicon tetrahedra is a reflection of the disorder associated with the bond-length and bond-angle distributions. Furthermore, the total number of such tetrahedra is indicative of the presence of coordination defects. For models with no coordination defects, all Si atoms are 4-fold coordinated, and the number of tetrahedra is equal to the number of Si atoms. Thus, the volume distribution of the tetrahedra can be considered as a form of reduced 4-body correlation function, which is sensitive to bond lengths, bond angles, and the coordination number of an atom.

Figure 6 shows various tetrahedral units formed by different silicon-hydrogen bonding configurations that can be used to represent the network structure of a-Si:H. Silicon and hydrogen atoms are shown in yellow and white colors. The volume distribution of these tetrahedra provides useful information regarding the change of the local structure and ordering associated with hydrogen passivation. Depending on the presence of mono-, di-, and trihydride configurations, the network may consist of Si_3H, Si_2H_2, and SiH_3 tetrahedra. The volume distributions of these tetrahedra for an a-Si:H model with 17.9 at. % H, along with a 1000-atom model of pure a-Si, are plotted in Fig. 7. The peak areas are proportional to the number of different $Si_{4-n}H_n$ tetrahedra for $n = 0$, 1,

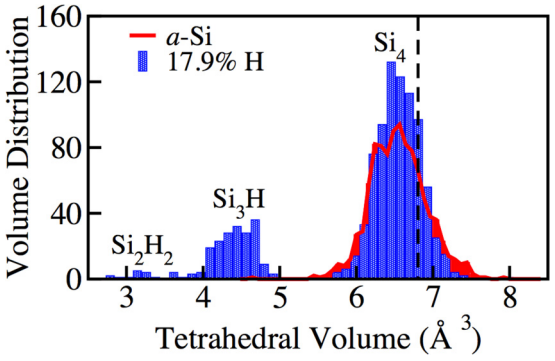

FIG. 7. The volume distributions of individual $Si_{4-n}H_n$ tetrahedra for a model of a-Si (red) and a-Si:H (blue). The contributions from different H-bonded tetrahedra (see Fig. 6) are indicated. The vertical line (at 6.8 Å^3) corresponds to the volume of an ideal Si_4 tetrahedron in the crystalline-silicon environment.

and 2. A careful examination of the distributions in Fig. 7 reveals a subtle change associated with the volume of primary Si_4 tetrahedra upon hydrogenation. The tetrahedral volume distribution of pure a-Si is slightly wider than its hydrogenated counterpart. This appears to suggest that the hydrogenation of a-Si not only passivates the dangling bonds but also modifies the entire network to produce a narrower distribution of primary (i.e., Si_4) tetrahedral volumes in a-Si:H. Since the volume distribution of Si_4 tetrahedra for a-Si is obtained from a 100% 4-fold CRN model of the highest quality [3], this small deviation can be seen as an indicator of the local changes associated with the Si_4 tetrahedra in a-Si:H. To treat both the data sets on an equal footing from a computational point of view, we have relaxed the CRN model of a-Si using a double-ζ basis in SIESTA. Finally, the volume of a perfect tetrahedron from the crystalline-silicon structure is indicated as a vertical line at 6.8 Å^3. Once again, we have relaxed the crystalline Si structure using a double-ζ basis in SIESTA for consistency in our calculations. The crystalline volume of 6.8 Å^3 corresponds to an equilibrium nearest-neighbor distance of 2.367 Å in the diamond structure.

B. Hydrogen distribution and NMR line spectra

In this section, we present an approximate calculation of the shape of nuclear magnetic resonance spectra for device-quality models (i.e., 7 to 14 at. % of H with a very few defects) of a-Si:H by examining the real-space distribution of H atoms, and compare the results with experimental NMR spectra [23–26]. Experimental data from NMR [23,24] and multiple-quantum NMR measurements [26] suggest that, at low concentrations, the dipolar interaction between spins (i.e., H nuclei) yields a narrow spectrum, which is often approximated by a Cauchy-like distribution near the resonance frequency. This indicates the presence of H atoms in a dilute or sparse environment. However, a broad spectrum results in high concentrations of hydrogen, which is generally interpreted as being due to the presence of small hydrogen clusters (4–8 H atoms) within a region of 3–5 Å radius [26,61]. To study the shape of the resonance curve, we have calculated the NMR spectra for two models with 6.9 and 14.7 at. % H using the Van Vleck moments [62] of the spin distribution [61]. In the moment-based approach, an NMR spectrum can be approximated as a linear combination of truncated Gaussian (broad) and Cauchy (narrow) distributions, which are defined via the first two nonzero Van Vleck moments. The distributions are weighted by appropriate mixing parameters, which are deduced from the number of hydrogen atoms present in the clustered and dilute phases in the model. The widths of the Gaussian and truncated Cauchy distributions are characterized by the second and fourth moments of the spin (H nuclei) distribution in real space. Following Van Vleck [62], the second and fourth moments of a system of N randomly distributed spins can be expressed as

$$\frac{\mu_2}{\gamma^4\hbar^2} = \frac{1}{2N}\sum_{i<j}^{N} b_{ij}^2, \tag{5}$$

$$\frac{\mu_4}{\gamma^8\hbar^4} = \frac{3}{16N}\sum_{\langle ikl\rangle}^{N} b_{ik}^2 b_{il}^2 - \frac{1}{36N}\sum_{\langle ikl\rangle}^{N} b_{ik}^2 (b_{il}-b_{kl})^2 + \frac{1}{72N}\sum_{\langle ikl\rangle}^{N} b_{ik}b_{kl}(b_{il}-b_{ik})(b_{il}-b_{kl}) + \frac{1}{8N}\sum_{i<k}^{N} b_{ik}^4, \tag{6}$$

where

$$b_{ij} = \frac{3}{2}\frac{(1-3\cos^2\theta_{ij})}{r_{ij}^3}$$

and θ_{ij} is the angle between the vector r_{ij} and the direction of the applied magnetic field. In Eq. (6), the symbol $\langle ikl\rangle$ implies a triple summation with no two indices being equal, and γ is the gyromagnetic ratio of hydrogen nuclei. For an ideal Gaussian function, $\Gamma = \mu_4/\mu_2^2 = 3$ and the full width at half maximum (FWHM) is given by $\sqrt{8\,\mu_2 \ln 2}$. This reflects a complete random distribution of spins at high concentration. Likewise, in the dilute limit, a random distribution of spins produces a narrow Lorentzian or Cauchy-like distribution near the resonance frequency. In practice, the shape of an experimental resonance curve is neither a Gaussian nor Lorentzian. The presence of correlation between hydrogen atoms, which is evidenced from the H-H pair-correlation function, modifies the resonance curve considerably and produces an intermediate shape between the two limits. To proceed further, we make the approximation that the resonance curve can be expressed as a linear combination of a Gaussian and a truncated Cauchy function [63]:

$$f(\nu) = \alpha f_g(\nu) + \beta f_l(\nu). \tag{7}$$

Here α and β are the parameters indicating the total fraction of clustered and dilute H atoms in our model a-Si:H networks, respectively, and $f_g(\nu)$ and $f_l(\nu)$ are the Gaussian and truncated Cauchy functions, respectively. In the spirit of the analysis of experimental IR data, we choose $\beta = 1-\alpha$. This is equivalent to the assumption that a hydrogen atom that does not belong to clusters contributes to the dilute phase. The functions $f_{g,l}(\nu)$ above are defined via the first two nonzero moments of the spin distribution. To calculate the configurational-average line spectra, we have used several magnetic field directions.

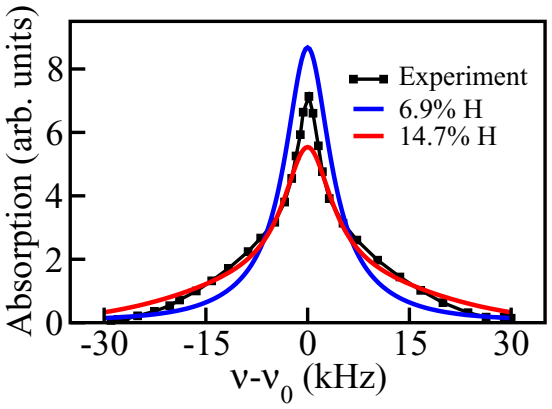

FIG. 8. Comparison of ^{1}H-NMR spectra from simulations (red and blue) and experiments (black). Simulated spectra correspond to *a*-Si:H models with 6.9 at. % (blue) and 14.7 at. % (red) of hydrogen. Experimental data are from Ref. [25] and correspond to a sample of *a*-Si:H with 10–15 at. % hydrogen.

It should be noted that the shape of the resonance curve obtained in this manner is an approximation of the true resonance curve, especially at very dilute concentrations, and that the experimental data can deviate significantly, depending on the concentration of hydrogen, history of the samples, and the degree of inhomogeneities associated with the distribution of hydrogen in the models. Furthermore, the spectrum constructed from the NMR moments is purely classical, which involves only the dipolar interaction between spins, and does not include any effect of the electron-mediated spin-spin interaction in solids. Additionally, the moment-based approach breaks down at very dilute concentrations when the resonance function is almost Lorentzian, leading to divergence of the second- and higher-order moments.

Figure 8 shows the calculated NMR spectra for two *a*-Si:H models with 6.9 at. % and 14.7 at. % of hydrogen, along with the experimental data from Ref. [25], which correspond to 10–15 at. % H. For comparison, the simulated data from Eq. (7) are multiplied by an appropriate normalization factor so that both the experimental and simulated data have an identical zeroth moment or area under the plots. Although the simulated spectra from the moment-based approach appear to deviate from the experimental data, this minor deviation is not unexpected in view of the approximate nature of the moment-based method. The reconstructed spectrum depends not only on the truncated distributions but also on the relative weight or the mixing parameter, α. The latter depends on the density of the clustered phase of H atoms, which characterizes the 3-dimensional distribution of hydrogen in *a*-Si:H. Figures 9 and 10 show several such clusters of hydrogen in a spherical region of radius 3.8–4 Å at low and high concentrations, respectively. The presence of such clusters, consisting of 5–8 H atoms in a spherical region of radius 3–5 Å, is consistent with the conclusions from nuclear magnetic resonance studies [23,24,26]. For clarity of visualization, a hypothetical Gaussian surface is shown around each cluster [64].

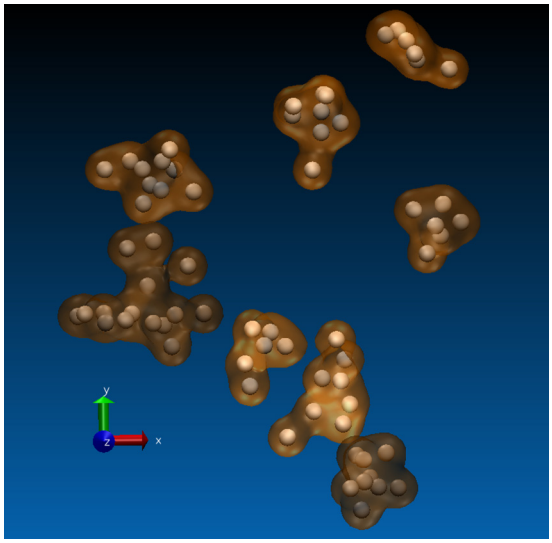

FIG. 9. Distribution of H clusters (white) in a 1000-Si-atom model with 17.9 at. % H. For visual clarity, individual clusters are enclosed within a hypothetical Gaussian isosurface (orange).

C. Hydrogen distribution: Density of clustered and isolated phases

In the preceding section, we have seen that the shape of the resonance curve provides useful information on the real-space distribution of H atoms in the network. However, since an NMR spectrum provides a one-dimensional representation of a hydrogen distribution, it cannot be used to uniquely characterize the full three-dimensional distribution of H atoms in real space. Further characterization of the hydrogen distribution is possible by comparing the distribution of Si-H bonding configurations in model networks with the results from IR measurements [19,21,22,42]. Experimentally, the frequencies associated with the stretching peaks in the IR spectra can be obtained via deconvolution of the high-frequency region of the

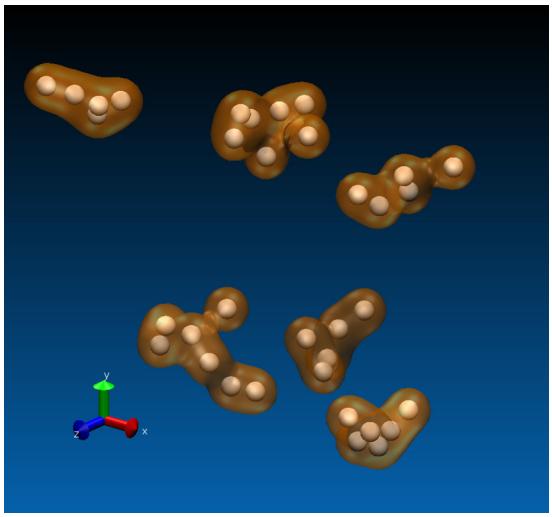

FIG. 10. A few H clusters (white) in a 1000-Si-atom model with 10.6 at. % H. For visual clarity, a hypothetical Gaussian isosurface (orange) is constructed around each cluster.

spectra using Gaussian functions. The hydrogen involvement in a vibrational mode is determined from the integrated absorption strength and the matrix element of the mode. Ouwens and Schropp [42] obtained estimates for the densities of clustered and isolated hydrogen atoms using different oscillator strengths and refractive indices of H atoms in the clustered and isolated phases. By analyzing the integrated absorption strengths of stretching modes at 2000 cm^{-1} and 2100 cm^{-1} from infrared measurements, these authors conclude that up to 4 at. % of total hydrogen can be dissolved into the amorphous matrix to form an isolated/distributed phase, which is independent of the methods of preparation and the deposition conditions of their samples. Similar conclusions followed from the work of Acco *et al.* [22], who studied the evolution of the hydrogen concentration profile and bonding configurations using secondary-ion-mass spectrometry and infrared spectroscopy.

To calculate the density of distributed H atoms in our models, we assume that a hydrogen atom is isolated if the atom does not have any hydrogen neighbor within a spherical region of radius 4–6 Å. While this particular range may appear to be somewhat empirical, it is motivated by our desire to compare the results with the experimental data from Ref. [42], where the authors obtained an average isolation radius of 5.9 Å based on the analysis of their experimental data using phenomenological arguments. Figure 11 presents the results for the percentage of isolated H atoms (with respect to total hydrogen) for two models with 10.6 at. % and 17.9 at. % of hydrogen for isolation radii between 4–6 Å. The results suggest that the density of isolated hydrogen atoms does not exceed 4 at. % of total hydrogen for a radius of 4 Å for a device-quality model with 10.6 at. % of H. Similarly, at high concentration, there are a few distributed H atoms (< 2%) present in the network. These results are consistent with the experimental results obtained by Acco *et al.* [22] and Ouwens and Schropp [42]. An example of

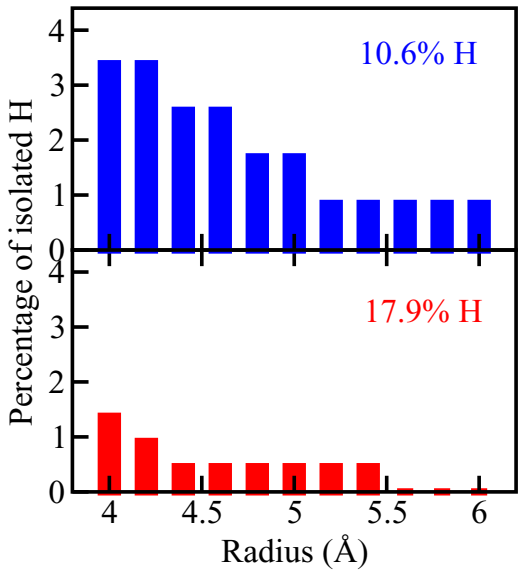

FIG. 11. Density of distributed H atoms (in percentage of total hydrogen) at low and high concentrations with a varying isolation radius. The hydrogen concentration of *a*-Si:H models is indicated in the plot.

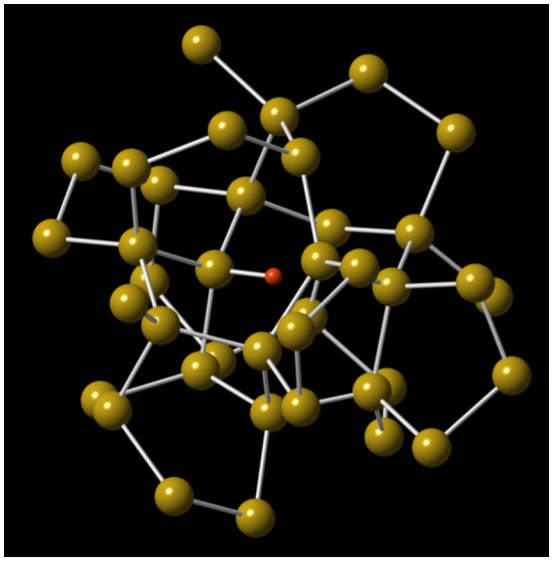

FIG. 12. An example of a distributed SiH configuration (red) in a 1000-Si-atom model of *a*-Si:H with 10.6 at. %. The radius of the spherical region shown above is 5.9 Å.

a distributed H atom (i.e., an isolated monohydride) is shown in Fig. 12 with an isolation radius of 5.9 Å. It may be noted that, for a perfectly homogeneous distribution consisting of N_h hydrogen atoms in volume V, the hydrogen-hydrogen separation cannot be more than $l_0 = \sqrt[3]{V/N_h}$. This translates into a maximal distributed radius of 4.3 Å and 6.9 Å for 22 at. % and 6.9 at. % of H, respectively. Since, for comparison with experimental data [42] $l_0 \gg 5.9$ Å, a condition that is not satisfied by the models at high concentrations of H, our results at high concentrations are somewhat affected by the small size of the models. Here, we have used a value of 4.5 Å as an isolation radius for the calculation of the density of isolated/distributed atoms.

The density of clustered hydrogen can be determined by introducing a suitable definition of hydrogen clusters. Following NMR studies [23], one may assume that a hydrogen atom belongs to a clustered phase if it is surrounded by at least $n_H = 5$–7 or more H atoms in a spherical region of $r_c = 3.5$–4.5 Å. For the present calculations, we have chosen a value of $n_H = 5$ H atoms and $r_c = 3.8$ Å to define a cluster. The latter is approximately equal to the average separation between two H atoms, which are bonded to two neighboring Si atoms, such as H-Si-Si-H (see Ref. [65]). The remaining H atoms are assumed to be distributed in a dilute or sparse phase, which is neither clustered nor isolated. The corresponding density of such a dilute phase can be obtained by subtracting the sum of distributed/isolated and cluster phases from the total density of H atoms. It may be noted that, depending on the definition of a cluster, a few small H clusters can reside in a dilute distribution of hydrogen. It is appropriate to mention at this point that IR studies often do not distinguish between isolated and dilute phases, an assumption that we have already employed in the reconstruction of an NMR spectrum. Hydrogen atoms, which are not isolated, contribute to the clustered phase [42]. Figure 13 shows the percentage of total H atoms that appear

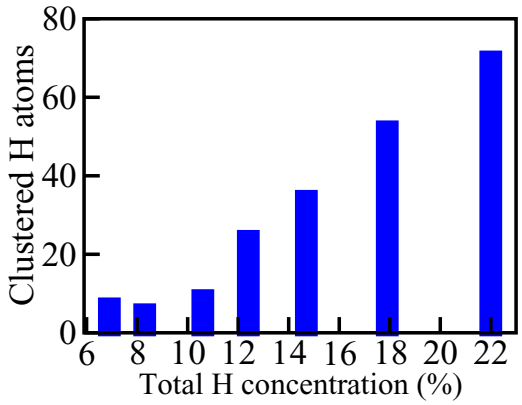

FIG. 13. Density of clustered H atoms (in percentage of total H) as a function of total H concentration for a set of a-Si:H models. A hydrogen cluster is defined as a group of five or more H atoms in a spherical region of radius 3.8 Å.

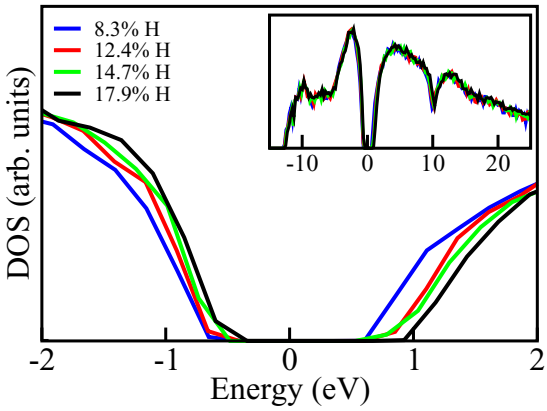

FIG. 14. Electronic density of states (DOS) of a-Si:H models in the vicinity of the band gap near the band edges for different hydrogen concentrations. The full valence and conduction bands are shown in the inset. The Fermi level is located at 0 eV.

in the clustered environment for different concentrations of hydrogen.

Table II provides the statistics of hydrogen distributions by listing the number density of H atoms in isolated ($C_{\rm iso}$) and clustered ($C_{\rm clus}$) phases with respect to total hydrogen content, as well as the percentage of H atoms ($M_{{\rm SiH}_n}$) associated with SiH_n bonding configurations. For the calculation of the density of isolated H atoms (in Table II), we have used a radius of 4.5 Å. Similarly, as mentioned in Ref. [65], a hydrogen cluster is defined as a group of 5 or more H atoms in a spherical radius of 3.8 Å. A comparison of $C_{\rm iso}$ between simulated values from Table II and experimental results from Refs. [22] and [42] suggests that our results are well within the range of experimental values obtained for device-quality models. The densities of H atoms (with respect to total H) associated with mono- and dihydride configurations are also listed in Table II as $M_{\rm SiH/SiH_2}$.

D. Electronic and optical properties

Having studied the structural properties of the models, we now address the electronic and optical properties. The optoelectronic properties crucially rely on the electronic density of states (EDOS). The band-gap region, in particular, is very sensitive to the concentration of defects and the degree of disorder in the networks. The presence of defects introduces gap states in the EDOS, whereas disorder influences the states near the valence- and conduction-band tails. These affect the optical and electronic properties of the material. For example, the size of the optical gap (obtained via Tauc plots [66]) and the electronic conductivity (obtained via the Kubo-Greenwood formalism) depend on the distribution of valence- and conduction-band tail states, and the magnitude of the gap. In Fig. 14, we have plotted the EDOS for four a-Si:H models with hydrogen concentrations of 8.3, 12.4, 14.7, and 17.9 at. % of hydrogen obtained from SIESTA using a double-ζ basis and the local density approximation (LDA) for the calculation of the exchange-correlation energy.

The absence of coordination defects in the hydrogenated models has produced a clean electronic gap of size ranging from 1.2 to 1.3 eV. This value is smaller than the optical gap of 1.61–1.72 eV extrapolated from the measured optical-absorption spectra for samples of a-Si:H with 6.5–21.8 at. % of hydrogen in Ref. [41]. The deviation from the experimental value can be attributed partly to the use of the LDA with localized basis functions and the variational nature of the density-functional calculations, and partly to the parametrization of the optical functions (e.g., the dielectric function) for fitting the optical-absorption data from experiments. The Tauc plot for the model with 12.4 at. % H is shown in Fig. 15. Due to reasonably large system sizes and the use of double-ζ basis functions, we have resorted to estimating the value of the optical gap by extrapolating the joint density of states (JDOS) using the parabolic approximation for the band edges and assumed an energy-independent transition matrix element between the valence and conduction bands. A linear least-squares fit of the JDOS from 1.5 eV to 4.5 eV yields an extrapolated value of 1.57 eV for the optical gap in Fig. 15. This value is somewhat smaller than the experimental value of 1.66 eV from Ref. [41] but larger than the value of 1.3 eV estimated from the EDOS (in Fig. 14). Since the latter reflects the energy difference between the highest occupied and lowest unoccupied energy states, it is often referred to

TABLE II. Statistics of hydrogen distribution in a-Si:H. System sizes (N), hydrogen concentration ($H_{\rm conc}$), hydrogen contents of SiH_n ($M_{{\rm SiH}_n}$), and clustered/isolated hydrogen $C_{\rm clus/iso}$ are listed. $M_{{\rm SiH}_n} = [\frac{nN_n}{N_h}] \times 100$, where N_n is the number of SiH_n configurations and N_h is the total number of H atoms.

N	ρ (g cm^{-3})	$H_{\rm conc}$ (at. %)	$M_{\rm SiH}$ (%)	$M_{\rm SiH_2}$ (%)	$M_{\rm SiH_3}$ (%)	$C_{\rm iso}$ (%)	$C_{\rm clus}$ (%)
1074	2.236	6.9	100	0	0	8.1	8.1
1090	2.233	8.3	96.7	3.3	0	5.55	6.6
1118	2.217	10.6	98.3	1.7	0	2.54	10.2
1142	2.205	12.4	97.9	2.1	0	4.22	25.3
1172	2.196	14.7	93.0	7.0	0	1.74	35.5
1218	2.174	17.9	87.2	12.8	0	0.46	53.2
1282	2.165	22.0	77.0	19.9	3.1	0.00	71.0

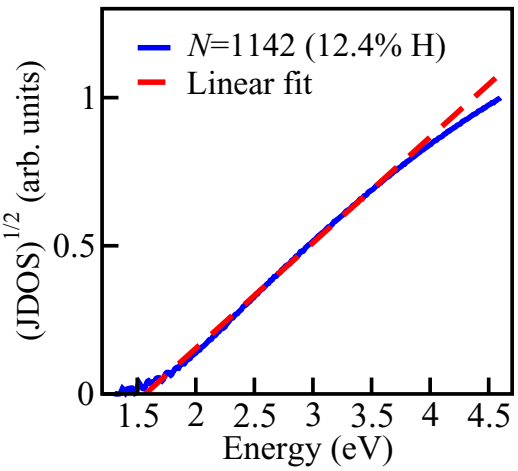

FIG. 15. A Tauc plot showing a linear extrapolation from the joint density of states (blue) to obtain an estimate of the optical gap (1.57 eV above) using a least-squares fit (red).

as the HOMO-LUMO gap, and is generally smaller than the optical gap due to the presence of a few defect states and the neglect of the energy-dependent transition matrix elements in the calculations.

An inspection of the EDOS in Fig. 14 shows a gradual widening of the gap with increasing hydrogen concentration except for the model with 8.3 at. % H. This is evident in Fig. 16, where we have plotted the size of the optical gap with hydrogen concentration for a set of a-Si:H models with 1000 Si atoms. This widening of the gap with increasing hydrogen concentration is consistent with the experimental results from photoelectron spectra by von Roedern and co-workers [67] and the dielectric measurements of a-Si:H using spectroscopic ellipsometry by Kageyama *et al.* [41]. The latter observed a shift of the entire dielectric function toward high energies with decreasing substrate temperature, which resulted in a linear increase of the optical gap of the samples with increasing hydrogen content. This observation is reflected qualitatively in Fig. 16, except for the model with 8.3 at. % of H, where

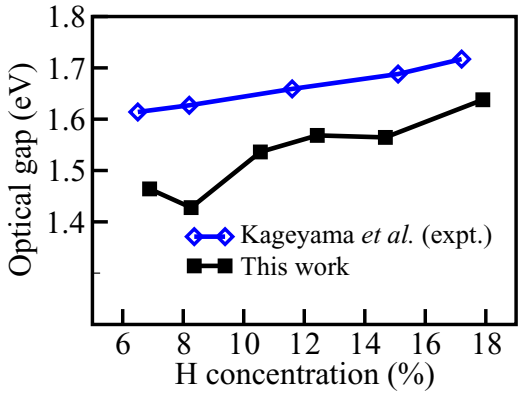

FIG. 16. Variation of the optical gap (obtained from the Tauc plot) in a-Si:H with hydrogen concentrations. The widening of the gap with increasing hydrogen concentration is consistent with experimental data in Refs. [41,67]. Experimental data shown above are from Ref. [41].

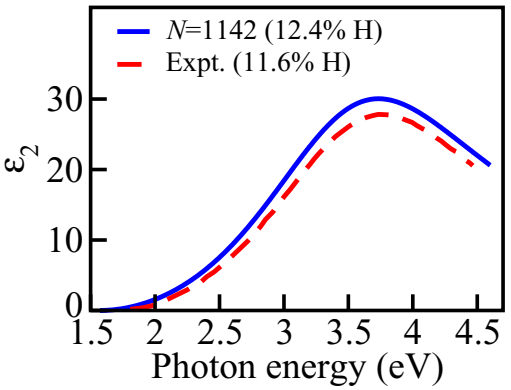

FIG. 17. Dielectric function of a-Si:H from experiments (red) and simulations (blue) using the Tauc-Lorentz model. Experimental data are from Ref. [41] and correspond to a sample with approximately 11.6 at. % of hydrogen.

the value of the optical gap (for the 1000-Si-atom model) has increased from 1.45 eV at 6.9 at. % H to 1.6 eV at 17.9 at. % of hydrogen. The widening of the band gap can be understood in terms of silicon-hydrogen bond formation with increasing hydrogen concentration. The addition of hydrogen causes a partial reduction of the states near the valence-band tail through the formation of SiH and SiH_2 configurations (see Fig. 14). Hydrogen passivates the defect states, located near the valence tail, by forming Si-H bonds through Si($3p$)-H($1s$) interactions [68]. These Si-H configurations reduce the local strain and disorder through the formation of the silicon-hydrogen bonding states lying deep in the valence band. An examination of the local EDOS associated with H-bonded silicon atoms confirms this observation.

The dielectric function of the a-Si:H model with 12.4 at. % H is plotted in Fig. 17 using the Tauc-Lorentz (TL) model [69]. In the TL model, the imaginary part of the dielectric function, $\epsilon_{2,TL}(E)$, is expressed as a product of the Tauc joint density of states [66] and the matrix element of a classical damped harmonic (Lorentzian) oscillator in the presence of an electromagnetic field [70]:

$$\epsilon_{2,TL}(E) = \begin{cases} \dfrac{AE_0C(E-E_g)^2}{\left(E^2-E_0^2\right)^2+C^2E^2}\dfrac{1}{E}, & E \geqslant E_g, \\ 0, & E < E_g, \end{cases} \quad (8)$$

where the parameters A, E_0, C, and E_g correspond to the amplitude, broadening, peak transition, and Tauc-Lorentz optical gap, respectively. For the purpose of calculating the imaginary part of the dielectric function, we have used the value of the optical gap $E_g = 1.57$ eV obtained from the joint density of states, and values of $A = 214.05$ eV, $C = 2.33$ eV, and $E_0 = 3.649$ from Ref. [41] for the sample with 11.6 at. % of hydrogen. Figure 17 shows the plot of the dielectric function $\epsilon_{2,TL}(E)$ as a function of photon energy E. The deviation from the experimental data near the peak-transition energy of $E_0 = 3.65$ eV can be understood by noting the behavior of $\epsilon_{2,TL}(E)$ near E_0. For $E = E_0$, $\epsilon_{2,TL}(E = E_0) = B(E_0 - E_g)^2$, where $B = A/CE_0$. Since E_g has been underestimated in our calculations, the deviation is more pronounced near the peak transition energy E_0, and decreases as E goes away

from the peak. By directly fitting the experimental data using Eq. (8), Kageyama *et al.* [41] reported a value of 1.66 eV for the optical gap for a sample with 11.6 at. % H, which is about 5.5% higher than the estimated value of 1.57 eV for the model with 12.4 at. % H obtained from the joint density of states in Fig. 15.

E. Vibrational properties

As a final test of our models, we briefly examine the vibrational properties of *a*-Si:H models by diagonalizing the dynamical matrix in the harmonic approximation [71]. Since vibrational modes in *a*-Si:H typically involve an excitation energy of several tens of meV (for bending modes) to a few hundreds of meV (for stretching modes), they are very sensitive to minute structural changes associated with the environment of silicon and hydrogen atoms. For example, the frequency positions and vibrational character of stretching modes (SMs) depend on the hydrogen contents of mono- and dihydride configurations and their local chemical environment. Infrared-absorption measurements suggest that the high-frequency region of the IR spectra in *a*-Si:H is characterized by the presence of a narrow band (2000–2040 cm^{-1}) of low-frequency stretching modes (LSMs), which is accompanied by a relatively broad band (2060–2250 cm^{-1}) of high-frequency stretching modes (HSMs) [72–74]. Although the assignment and the origin of these modes are still not very clear, it is now widely accepted that monohydrides (SiH) are largely responsible for the LSMs [22,38,42,74], whereas the contributions to the HSMs come from dihydrides and a few monohydrides on internal surfaces or voids [41,75]. Figure 18 shows the vibrational density of states of a device-quality model with 12.4 at. % H along with the experimental data from inelastic neutron-scattering experiments [76] on *a*-Si, and infrared-absorption measurements [21] on *a*-Si:H at room temperature. The high-frequency region of the vibrational spectrum shows the presence of two distinct bands: (1) a narrow band from 1960 to 2020 cm^{-1}; (2) a wide band from 2040–2180 cm^{-1}. A real-space analysis of the eigenvectors, in the frequency range 2040–2120 cm^{-1}, obtained from the dynamical matrix of the model with 12.4 at. % H indicates that these modes have 100% stretching character and originate from both monohydride and dihydride configurations. The localization character of the vibrational eigenvectors (i.e., normal modes) follows directly from the inverse participation ratio (IPR):

$$\mathrm{IPR}(\nu) = \sum_{i=1}^{N} \left[\phi_{i_x}^2 + \phi_{i_y}^2 + \phi_{i_z}^2\right]^2, \tag{9}$$

where ϕ_{i_x}, ϕ_{i_y}, and ϕ_{i_z} are the x, y, z components of the normalized eigenvector $\phi(\nu)$ or normal mode of frequency ν projected on atom i and N is the total number of atoms in the system. For a completely localized mode, centered on a single atom, IPR = 1, whereas for an ideal extended mode distributed over all atoms, IPR = $1/N$. The plot of the IPR versus frequency (in cm^{-1}) is shown in the lower panel of Fig. 18. An analysis of the vibrational modes suggests that most of the high-frequency stretching modes are strongly localized in character (with IPR $\geqslant$ 0.9). Figure 19 shows an example of such a high-frequency stretching mode (HSM) associated with an isolated monohydride configuration observed in a model of *a*-Si:H with 12.4 at. % of hydrogen. The frequency of the mode is given by 2182 cm^{-1}. The mode is found to be highly localized in real space with an IPR value of 0.95. An analysis of the eigenvector associated with this mode confirms that the mode is 100% stretching in character, and that the

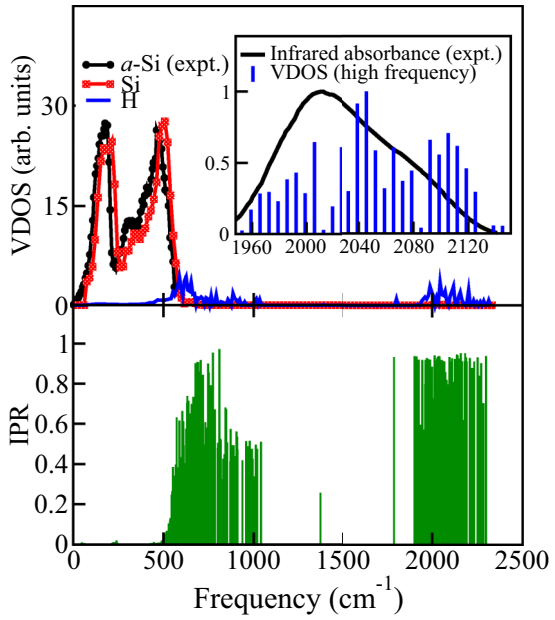

FIG. 18. Atom-projected vibrational density of states of a 1000-Si-atom model of *a*-Si:H with 12.4 at. % H along with the inelastic neutron-scattering data (black) from Ref. [76]. The inset shows the calculated high-frequency vibrational modes and the experimental IR spectrum of *a*-Si:H from Ref. [21]. The lower panel shows the inverse participation ratio (IPR) of the vibrational eigenstates as a function of frequency.

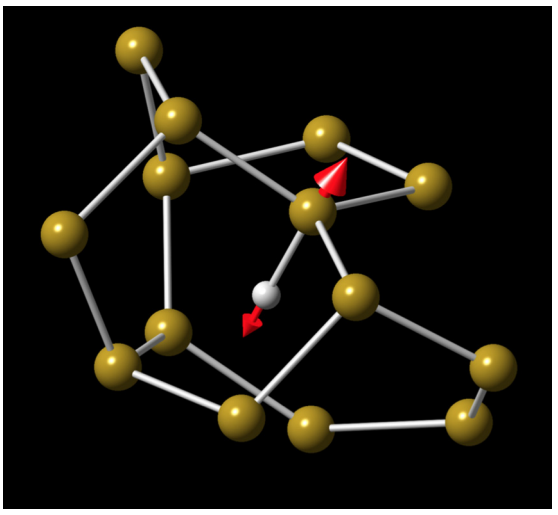

FIG. 19. A high-frequency stretching mode ($\nu = 2182$ cm^{-1}) associated with an isolated monohydride configuration in a model of *a*-Si:H with 12.4 at. % of hydrogen. The vibrational motion associated with this mode is found to be highly localized (with an IPR value of 0.95) and centered on the hydrogen (white) and silicon (yellow) atoms of the Si-H bond as indicated.

vibrational motion (of atoms) associated with this mode is mostly confined to the hydrogen and silicon atoms of the Si-H bond as shown in Fig. 19. Similar observations have been found to be true for other high-frequency modes. Thus, our models correctly produce the characteristic frequency positions of H atoms, the nature of the vibrational modes, and the localized character associated with these frequencies, which have been observed in infrared absorption and inelastic neutron scattering experiments. The low-frequency localized modes are mostly due to various bond-bending vibrational configurations involving Si-H bonds.

IV. CONCLUSIONS

We have presented a dynamical approach to generate continuous-random-network models of *a*-Si:H by combining classical metadynamics with first-principles molecular-dynamics simulations and total-energy relaxations. Unlike conventional MD simulations of amorphous solids, where the absence of strong glassy behavior produces too many defects, the present approach provides a way to control the concentration of coordination defects by using the atomic coordination of constituent atoms as collective variables along with few configurational constraints in metadynamical simulations. The ability to control defect concentrations using collective variables makes it possible to generate nearly 100% defect-free models of *a*-Si:H via subsequent hydrogen passivation. A comparison with the existing simulation methods reveals the following advantages of our approach: (1) The method provides a systematic way to generate large defect-free models of *a*-Si:H over a wide range of concentrations. (2) It produces a hydrogen microstructure by passivating a random distribution of defects in *a*-Si networks. This eliminates any spurious correlations in the hydrogen distribution, which might appear in approaches based on the direct insertion of H atoms via the breaking of weak Si-Si bonds or the incorporation of experimental data in the generation of models. (3) The density and distribution (i.e., isolated versus clustered) of silicon-hydrogen configurations can be controlled quite accurately by using appropriate configurational constraints in order to study their effects on electronic and vibrational properties. (4) The method can be readily employed to generate structural models of binary/ternary amorphous networks and amorphous-crystalline heterojunctions for which reliable classical/semiclassical potentials are available. For multinary amorphous solids, the approach can be extended to include *ab initio* force fields in metadynamical simulations.

An examination of structural, electronic, optical, and vibrational properties of the models suggests that they are in excellent agreement with experimental data from infrared, nuclear magnetic resonance, inelastic neutron scattering, and optical absorption studies. The microstructure of hydrogen distributions in the models is characterized by the presence of isolated and clustered H phases in the background of an intermediate phase of hydrogen. Approximately 0.5–8 at. % of total hydrogen atoms have been found to occur in an isolated environment, which is comparable with the experimental values of 0–4.5 at. % H inferred from infrared spectroscopy [22,42]. The results are more-or-less consistent with experimental data, taking into account the limits of our simulations. The density of clustered hydrogen shows a monotonic increase with an increase in the hydrogen concentration. This agrees well with the data from optical-absorption measurements, which show an almost linear increase of the density (of the clustered phase) with hydrogen concentration. In conclusion, the metadynamical approach presented here provides an efficient way of producing large, high-quality, defect-free models of amorphous solids for further study of their structural, electronic, optical, and vibrational properties.

ACKNOWLEDGMENTS

The work used resources at the Texas Advanced Computing Center and the supercomputing facilities at the University of Texas at Arlington. R.A.-F. thanks Antonia M. Assimeh for her invaluable support. P.B. thanks the Department of Chemistry, University of Cambridge, for hospitality during an extended academic visit in 2015 when the work was initiated. The work is partially supported by NSF under Grants No. DMR 1507166 and No. DMR 1507118.

[1] W. H. Zachariasen, J. Am. Chem. Soc. **54**, 3841 (1932).
[2] F. Wooten, K. Winer, and D. Weaire, Phys. Rev. Lett. **54**, 1392 (1985).
[3] G. T. Barkema and N. Mousseau, Phys. Rev. Lett. **77**, 4358 (1996).
[4] D. A. Drabold, P. A. Fedders, S. Klemm, and O. F. Sankey, Phys. Rev. Lett. **67**, 2179 (1991).
[5] B. Tuttle and J. B. Adams, Phys. Rev. B **57**, 12859 (1998).
[6] P. Klein, H. M. Urbassek, and T. Frauenheim, Phys. Rev. B **60**, 5478 (1999).
[7] K. Jarolimek, R. A. de Groot, G. A. de Wijs, and M. Zeman, Phys. Rev. B **79**, 155206 (2009).
[8] F. Buda, G. L. Chiarotti, R. Car, and M. Parrinello, Phys. Rev. B **44**, 5908 (1991).
[9] R. A. Street, *Hydrogenated Amorphous Silicon* (Cambridge University Press, Cambridge, UK, 1991).
[10] K. Morigaki, *Physics of Amorphous Semiconductors* (Imperial College Press, London, UK, 1991).
[11] A. V. Shah, H. Schade, M. Vanecek, J. Meier, E. Vallat-Sauvain, N. Wyrsch, U. Kroll, C. Droz, and J. Bailat, Prog. Photovoltaics **12**, 113 (2004).
[12] B. Fiéque, J. Tissot, C. Trouilleau, A. Crastes, and O. Legras, Infrared Phys. Technol. **49**, 187 (2007).
[13] T. Mishima, M. Taguchi, H. Sakata, and E. Maruyama, Sol. Energy Mater. Sol. Cells **95**, 18 (2011).
[14] M. Taguchi, A. Yano, S. Tohoda, K. Matsuyama, Y. Nakamura, T. Nishiwaki, K. Fujita, and E. Maruyama, Photovoltaics, IEEE Journal of **4**, 96 (2014).
[15] K. Masuko, M. Shigematsu, T. Hashiguchi, D. Fujishima, M. Kai, N. Yoshimura, T. Yamaguchi, Y. Ichihashi, T. Mishima, N. Matsubara, T. Yamanishi, T. Takahama, M. Taguchi, E. Maruyama, and S. Okamoto, Photovoltaics, IEEE Journal of **4**, 1433 (2014).

[16] H. Takatsuka, Y. Yamauchi, K. Kawamura, H. Mashima, and Y. Takeuchi, Thin Solid Films **506**, 13 (2006).

[17] C. Micheletti, A. Laio, and M. Parrinello, Phys. Rev. Lett. **92**, 170601 (2004).

[18] A. Laio and M. Parrinello, Proc. Natl. Acad. Sci. USA **99**, 12562 (2002).

[19] C. Manfredotti, F. Fizzotti, M. Boero, P. Pastorino, P. Polesello, and E. Vittone, Phys. Rev. B **50**, 18046 (1994).

[20] H. Touir, K. Zellama, and J.-F. Morhange, Phys. Rev. B **59**, 10076 (1999).

[21] R. J. Scharff and S. D. McGrane, Phys. Rev. B **76**, 054301 (2007).

[22] S. Acco, D. L. Williamson, P. A. Stolk, F. W. Saris, M. J. van den Boogaard, W. C. Sinke, W. F. van der Weg, S. Roorda, and P. C. Zalm, Phys. Rev. B **53**, 4415 (1996).

[23] J. A. Reimer, R. W. Vaughan, and J. C. Knights, Phys. Rev. Lett. **44**, 193 (1980).

[24] D. J. Leopold, J. B. Boyce, P. A. Fedders, and R. E. Norberg, Phys. Rev. B **26**, 6053 (1982).

[25] W. E. Carlos and P. C. Taylor, Phys. Rev. B **26**, 3605 (1982).

[26] J. Baum, K. K. Gleason, A. Pines, A. N. Garroway, and J. A. Reimer, Phys. Rev. Lett. **56**, 1377 (1986).

[27] B. J. Min, Y. H. Lee, C. Z. Wang, C. T. Chan, and K. M. Ho, Phys. Rev. B **45**, 6839 (1992).

[28] J. M. Holender, G. J. Morgan, and R. Jones, Phys. Rev. B **47**, 3991 (1993).

[29] P. Biswas, R. Atta-Fynn, and D. A. Drabold, Phys. Rev. B **76**, 125210 (2007).

[30] P. Biswas, R. Atta-Fynn, and D. A. Drabold, Phys. Rev. B **69**, 195207 (2004).

[31] P. Biswas and S. R. Elliott, J. Phys.: Condens. Matter **27**, 435201 (2015).

[32] P. Biswas, D. A. Drabold, and R. Atta-Fynn, J. Appl. Phys. **116**, 244305 (2014).

[33] P. A. Fedders, Phys. Rev. B **61**, 15797 (2000).

[34] A. J. Franz, M. Mavrikakis, and J. L. Gland, Phys. Rev. B **57**, 3927 (1998).

[35] H. M. Branz, S. Asher, H. Gleskova, and S. Wagner, Phys. Rev. B **59**, 5513 (1999).

[36] G. N. van den Hoven, Z. N. Liang, L. Niesen, and J. S. Custer, Phys. Rev. Lett. **68**, 3714 (1992).

[37] P. Biswas and R. Timilsina, J. Phys.: Condens. Matter **23**, 065801 (2011).

[38] A. H. M. Smets and M. C. M. van de Sanden, Phys. Rev. B **76**, 073202 (2007).

[39] D. Williamson, A. Mahan, B. Nelson, and R. Crandall, J. Non-Cryst. Solids **114**, 226 (1989).

[40] A. C. Wright, A. C. Hannon, R. N. Sinclair, T. M. Brunier, C. A. Guy, R. J. Stewart, M. B. Strobel, and F. Jansen, J. Phys.: Condens. Matter **19**, 415109 (2007).

[41] S. Kageyama, M. Akagawa, and H. Fujiwara, Phys. Rev. B **83**, 195205 (2011).

[42] J. D. Ouwens and R. E. I. Schropp, Phys. Rev. B **54**, 17759 (1996).

[43] The nearest-neighbor function $\Theta(r)$ should be such that it is sufficiently smooth and decays rapidly between the first and second shell of neighbors as observed in the experimental pair-correlation data. This eliminates any possible discontinuity associated with the Gaussian forces and takes into account the contribution from the atoms that reside between the first- and second-neighbor shells at the beginning of metadynamical simulations from a random configuration. The cutoff values should be chosen accordingly.

[44] F. H. Stillinger and T. A. Weber, Phys. Rev. B **31**, 5262 (1985).

[45] R. L. C. Vink, G. T. Barkema, W. F. van der Weg, and N. Mousseau, J. Non-Cryst. Solids **282**, 248 (2001).

[46] S. Nosé, J. Chem. Phys. **81**, 511 (1984).

[47] W. G. Hoover, Phys. Rev. A **31**, 1695 (1985).

[48] G. J. Martyna, M. E. Tuckerman, D. J. Tobias, and M. L. Klein, Mol. Phys. **87**, 1117 (1996).

[49] Since the set of a-Si configurations collected during metadynamic simulations does not include any 5-fold over-coordinated bonds, the average value of ξ is always less than or equal to 4. For example, a configuration consisting of 77% 4-fold, 21% 3-fold, and 2% 2-fold Si atoms has an average coordination number $\xi = 0.77 \times 4 + 0.21 \times 3 + 0.02 \times 2 = 3.75$.

[50] The bond length of a newly constructed Si-H bond (upon hydrogenation) should not be too short or too long. A small value can induce instability in the atomic dynamics by increasing the potential energy of the system, whereas a large value can produce artifacts, such as the formation of new 5-fold defects, by H atoms being too close to a neighboring Si atom. A choice of 1.0–1.2 Å has been found to be optimal for the system to adjust the average Si-H bond length to be 1.5 Å during the *ab initio* molecular dynamics simulations.

[51] J. M. Soler, E. Artacho, J. D. Gale, A. Garciá, J. Junquera, P. Ordejón, and D. Sánchez-Portal, J. Phys.: Condens. Matter **14**, 2745 (2002).

[52] J. P. Perdew and A. Zunger, Phys. Rev. B **23**, 5048 (1981).

[53] N. Troullier and J. L. Martins, Phys. Rev. B **43**, 1993 (1991).

[54] L. Kleinman and D. M. Bylander, Phys. Rev. Lett. **48**, 1425 (1982).

[55] J. Harris, Phys. Rev. B **31**, 1770 (1985).

[56] Z. Remeš, M. Vaněček, A. H. Mahan, and R. S. Crandall, Phys. Rev. B **56**, R12710 (1997).

[57] R. Atta-Fynn, P. Biswas, P. Ordejón, and D. A. Drabold, Phys. Rev. B **69**, 085207 (2004).

[58] N. Mousseau and L. J. Lewis, Phys. Rev. B **43**, 9810 (1991).

[59] K. Laaziri, S. Kycia, S. Roorda, M. Chicoine, J. L. Robertson, J. Wang, and S. C. Moss, Phys. Rev. Lett. **82**, 3460 (1999).

[60] S. R. Elliott, *Physics of Amorphous Materials* (Longman Scientific and Technical, Essex, England, 1990).

[61] R. Timilsina and P. Biswas, J. Phys.: Condens. Matter **25**, 165801 (2013).

[62] J. H. Van Vleck, Phys. Rev. **74**, 1168 (1948).

[63] A. Abragam, *Principles of Nuclear Magnetism* (Oxford University Press, Oxford, UK, 1994).

[64] A Gaussian isosurface can be constructed as a linear combination of three-dimensional Gaussian functions centered on the position of H atoms. The Gaussian decay constant is generally chosen to be a fraction of the nearest-neighbor distance between two H atoms. An appropriate isovalue can be chosen by trial and error.

[65] Given two Si atoms, which are bonded to each other and each having at least one hydrogen neighbor (e.g., H-Si-Si-H), the average distance between the H atoms is given by $R_{\text{H-H}} \approx R_{\text{SiH}} + R_{\text{H-Si-Si}} = 1.5$ Å + 2.3 Å = 3.8 Å. Here, R_{SiH}

is the average bond length of Si-H bonds and $R_{\text{H-Si-Si}}$ is the average second-neighbor distance between H and Si atoms (as in H-Si-Si). This value of $R_{\text{H-H}}$ is close to the radii of the H clusters, 3.5–4.5 Å, deduced from NMR experiments and is used as a characteristic radius of H clusters. Other values between 3.5–4.5 Å are equally acceptable and can be used to identify clusters.

[66] J. Tauc, R. Grigorovici, and A. Vancu, Phys. Status Solidi B **15**, 627 (1966).

[67] B. von Roedern, L. Ley, and M. Cardona, Phys. Rev. Lett. **39**, 1576 (1977).

[68] W. Y. Ching, D. J. Lam, and C. C. Lin, Phys. Rev. B **21**, 2378 (1980).

[69] G. E. Jellison and F. A. Modine, Appl. Phys. Lett. **69**, 371 (1996).

[70] F. Wooten, *Optical Properties of Solids* (Academic Press, New York, 1972).

[71] M. T. Dove, *Introduction to Lattice Dynamics* (Cambridge University Press, Cambridge, UK, 2005).

[72] M. Cardona, Phys. Status Solidi B **118**, 463 (1983).

[73] M. H. Brodsky, M. Cardona, and J. J. Cuomo, Phys. Rev. B **16**, 3556 (1977).

[74] A. A. Langford, M. L. Fleet, B. P. Nelson, W. A. Lanford, and N. Maley, Phys. Rev. B **45**, 13367 (1992).

[75] S. Guha, J. Yang, S. J. Jones, Y. Chen, and D. L. Williamson, Appl. Phys. Lett. **61**, 1444 (1992).

[76] W. A. Kamitakahara, H. R. Shanks, J. F. McClelland, U. Buchenau, F. Gompf, and L. Pintschovius, Phys. Rev. Lett. **52**, 644 (1984).